Original Article

A different zirconia precursor for Li$_7$La$_3$Zr$_2$O$_{12}$ synthesis

Check for updates

Fitria Rahmawati [a,*], Bilqies Musyarofah [a],
Khoirina D. Nugrahaningtyas [a], Anton Prasetyo [b], Veinardi Suendo [c,d],
Hery Haeruddin [e], Muhammad F.A. Handaka [e], Hanida Nilasari [e],
Hartoto Nursukatmo [e]

[a] Research Group of Solid State Chemistry & Catalysis, Chemistry Department, Sebelas Maret University, Jl. Ir. Sutami 36 A Kentingan,Surakarta, 57126, Indonesia
[b] Chemistry Department, UIN Maulana Malik Ibrahim, Malang, Indonesia
[c] Inorganic and Physical Chemistry Research Group, Chemistry Department,Faculty of Mathematics and Natural Sciences, Institut Teknologi Bandung, Bandung, Indonesia
[d] Research Centre for Nanoscience and Nanotechnology, Institut Teknologi Bandung, Bandung, Indonesia
[e] PDSMR Pertamina, Kawasan Mega Kuningan, Jakarta, Selatan, 12950, Indonesia

ARTICLE INFO

ABSTRACT

Li$_7$La$_3$Zr$_2$O$_{12}$ (LLZO) is a promising solid electrolyte for all-solid-state lithium-ion batteries. Some studies on LLZO synthesis have been conducted without considering the crystal structure of ZrO$_2$ as the main precursor. In this research, different-precursors have been used for LLZO synthesis which was a monoclinic ZrO$_2$ powder (m-ZrO$_2$) and tetragonal ZrO$_2$ powder (t-ZrO$_2$). The reaction was conducted at 950 °C 6 h and followed by sintering at 1000 °C 6 h under Argon gas flow. The result shows that LLZO made from m-ZrO$_2$ (LLZO(A)) and t-ZrO$_2$ (LLZO(B)) contains t-LLZO and c-LLZO which is surprisingly having a similar c/t ratio of 0.124—0.125. The LLZO(A) and LLZO(B) provide a silver blocking ionic conductivity of 1.245 x 10^{-6} Scm^{-1} and 1.647 x 10^{-6} Scm^{-1}, respectively. In addition, LLZO(B) provides lower specific resistance than LLZO(A) in between LiCoO$_2$ and meso-carbon microbeads (mcmb) electrodes. CV analysis of the symmetrical Li-LLZO(B)—Li cell shows an electrochemical potential of 3.3 V (vs Li/Li$^+$) oxidation and 3.4 V reduction (vs Li/Li$^+$). A time-based Galvanostatic charge—discharge to Li-LLZO(B)—Li shows a capacity drop after the 1st 40 cycles from 0.0383C/cm^2 into 0.0303C/cm^2 during the 2nd 40 cycles, and it remains stable up to 120 cycles. It confirms the long-term electrochemical stability of LLZO(B) which was produced from t-ZrO$_2$. The solid-state reaction method provides less expensive production and environmentally friendly by the absence of organic solvent.

1.   Introduction

In a Lithium-Ion Battery (LIBs), the electrolyte has a significant role to determines the stability, energy density, cycle life, and energy capacity of the battery. Within the electrolyte, Li^+ ions migrate in between anode—cathode [1,2]. The disadvantage of liquid electrolyte including vaporization, unstable at high temperature causing an explosion, and low cycle life [3] has driven the development of solid electrolyte. LIB with solid electrolyte or it is known as an all-solid-state lithium-ion battery (ASS LIB) has high thermal stability and low risk of explosion [4]. The solid electrolyte must have high Li^+ conductivity at least 1×10^{-4} Scm^{-1} with a low activation energy of Li^+ diffusion, be reliable for mass-production with a simple method, and have inexpensive precursors for its synthesis [5]. The $Li_7La_3Zr_2O_{12}$ (LLZO) is known as the best electrolyte for ASS-LIB due to its high ionic conductivity at room temperature, good stability in the air [6], and simple way to prepare [7]. Some methods that have been investigated are the sol—gel method, Pechini, co-precipitation, and solid-state reaction [8]. The sol—gel method produced a high purity LLZO with homogenous - small particles, however, the ionic conductivity of the after sintered material is only 10^{-7} Scm^{-1} with the sintering temperature of 800 °C [9]. Low ionic conductivity of 10^{-7} Scm^{-1} is also found with the LLZO produced by the Pechini method [9]. Meanwhile, even though the co-precipitation method could produce LLZO with the conductivity of 10^{-4} Scm^{-1}, however, this method requires solvents such as ammonium bicarbonate solution [10] which will be costly for mass-production, and the presence of side products is also being a problem. A solid-state reaction is a simple method without any required solvent. Therefore, the production cost can be reduced. The organic solvent — liquid waste also can harm the environment especially when mass production is applied.

A solid-state reaction with a sintering temperature of 1200 °C under an air atmosphere has successfully produced cubic garnet LLZO [7]. Meanwhile, a solid-state reaction with a sintering temperature of 1000 °C under an argon atmosphere produced a tetragonal LLZO [11]. Both researchers used ZrO_2 powder as Zr precursor, with the specification of ZrO_2 powder (Aldrich with >99% of purity) [7,12], and ZrO_2 powder (TOSOH) without any purity information. Both of the previous researches did not inform the crystal structure of the ZrO_2. Even though, the heating treatment is an important factor to determine the crystal structure of the product, including the temperature and the heating atmosphere as well. However, the crystal structure of the precursor may be another important factor. It is known that zirconia, ZrO_2 is formed within a monoclinic structure at 1000 °C and tetragonal at 1100—1200 °C. Tetragonal ZrO_2 has a smaller crystallite size than the monoclinic one. Small crystallite size could decrease the surface energy and reduce the internal stress allowing lower surface energy. Surface energy is a driving force during the sintering process [13], therefore crystal structure is an important factor for the synthesis result.

Regarding the discussion above, this research investigated whether the different crystal structures of ZrO_2 affect the $Li_7La_3Zr_2O_{12}$ synthesis, including its crystal structure, surface morphology, particle size, and its Li^+ conduction. Monoclinic ZrO_2 powder and tetragonal ZrO_2 powder were used by applying a low sintering temperature of 1000 °C under an Ar atmosphere [11]. The sintering method was chosen according to its lower temperature, which means lower cost, and to investigate whether the result would be a single tetragonal phase as mention previously [11] or it would depend on the crystal structure of the precursors.

2.   Methods

$Li_7La_3Zr_2O_{12}$ was synthesized by a solid-state reaction from La_2O_3 (95%, Merck), Li_2CO_3 (99%, Merck), and ZrO_2 as precursors. Two types of ZrO_2 used were monoclinic ZrO_2 (m-ZrO_2) powder (procured from XFNANO, China), and ZrO_2 powder (t-ZrO_2) that was produced by caustic fusion of $ZrSiO_4$ followed by heating at 1000 °C [14]. Both ZrO_2 powders were analyzed by X-ray Diffraction (XRD) (PANalytical Expert Pro, Cu radiation source), X-ray Fluorescence (XRF) (Bruker S2 Ranger). The Li_2CO_3 and ZrO_2 were heated at 900 °C for 1 h before being used in the reaction. Then, a stoichiometric weight of Li_2CO_3, La_2O_3, and ZrO_2 (weighed by Analytic Balance BOECO, Germany, max weight of 120 g, and accuracy of 0.0001 g) was mixed in a ball mill (MSK-SFM-3) for 8 h and 450 rpm with isopropanol as a dispersant.

The heated powder of Li_2CO_3 was poured into the reaction mixture at an extra 10% of stoichiometric weight to compensate for Li vaporization during calcination. The mixture powder was then calcined at 950 °C for 6 h. After calcination, the powder was re-milled within a ball milling for 12 h at 450 rpm. The resulted-powder was pressed with a hydraulic press at 166 MPa, then was sintered at 1000 °C in a tube furnace (EDULab Indonesia) with a heating rate of 20 ± 2.5 °C/min and cooling rate of 20 ± 2.5 °C/min [11]. Argon gas has flowed into the furnace during heating treatment. The result was pellets of LLZO from m-ZrO_2 (LLZO(A)), and the LLZO from t-ZrO_2 (LLZO(B)). The results were analyzed by X-ray diffraction (XRD) (PANalytical Expert Pro) equipped with Le Bail refinement within RIETICA software (a free edition) to understands the specific peaks compared to the standard diffraction of LLZO, surface morphology analysis, and elemental analysis with Scanning Electron Microscope/Energy Dispersive X-ray (SEM/EDX) (VEGA 3 TESCAN) and Raman analysis (BRUKER Senterra Spectrometer, resolution of 4 cm^{-1}, excitation wavelength source of 785 nm) to investigate the specific vibrations. Crystallite size was calculated from XRD data by applying Scherrer's equation as follows (Eq. (1)),

$$d = \frac{\kappa\lambda}{B\cos\theta} \quad ; \quad B = \frac{FWHM \cdot \pi}{180} \tag{1}$$

In which d is the mean crystallite size of the ordered domain (nm), κ is a dimensionless shape factor, λ is the X-ray wavelength (Cu radiation), 1.5409 Å, B is line broadening at Full-Width Half Maximum (FWHM) of the diffraction data, and θ is the Bragg angle [15].

Impedance analysis was conducted with an LCR meter (EUCOL U-2826, 20 Hz—5 MHz) by two methods of silver blocking and a wafer of meso-carbon microbeads (mcmb)| LLZO| $LiCoO_2$ (LCO). The Li^+ ions conductivity was calculated

based on the impedance data fitting with ZView (embedded within CS studio-5 a software of Corrtest Electrochemical Workstation). Blocking impedance analysis was conducted by paint a silver paste on both surfaces of the sintered-LLZO pellet. The green pellet was made by a hydraulic press (MELZER with pump Barton Tools, 0—40 MPa) at 5 metric tons and followed by cold isostatic pressure (Shanghai Wenqi Electric & Technology Co. Ltd, 0—40 MPa) at 20 MPa. The pellet was then sintered at 900 °C for 12 h. A silver wire was attached with silver paste on both surfaces as the current collector.

The wafer of mcmb | LLZO | LCO was prepared by casting mcmb slurry on Cu foil. The slurry was made by mixing the mcmb powder 94.5 wt % with acetylene black 1 wt %, CMC (Carboxy Methyl Cellulose), and styrene-butadiene rubber as the binder. The slurry was cast on Cu foil at 100 mm thickness and then dried within a vacuum oven at 120 °C for 24 h [16]. LLZO slurry was prepared by mix the LLZO powder with Polyvinilidenefluoride (PVDF, PT KGC Saintifik Indonesia) underweight ratio of 94.5%: 5.5%. The mixture was dispersed in N-methyl-2-pyrrolidine (NMP, PT KGC Saintifik Indonesia) until homogenous [3]. The homogenous slurry was then cast on Cu/MCMB by a tape casting method with a thickness of 0.32 ± 0.015 mm. After casting, the Cu/mcmb-LLZO was dried in a vacuum oven at 60 °C for 1 h. After cooled down to Room Temperature (RT), the second LLZO layer was cast on the first LLZO layer, and similarly was dried in a vacuum oven.

LiCoO$_2$ slurry was made by mix the LiCoO$_2$ powder (Sigma Aldrich) with PVDF and acetylene black under a ratio of 7:2:1 with NMP as a dispersant. The mixture was mixed for a night until homogenous and then was cast on Cu/mcmb | LLZO that was made before, to produce a wafer of Cu/mcmb| LLZO| LCO, then was dried within a vacuum oven at 60 °C for 1 h. The dried wafer was then punched with an electrode puncher to produce a circle wafer with a diameter of 1 cm. After punching, the Cu foil could be easily detached from mcmb surface. A silver wire was connected to the mcmb side and LCO side with silver paint and then was cured at 60 °C for 1 h the full cell was then vacuum wrapped and it was ready for analysis.

The asymmetric cell was made from the sintered-LLZO pellet with lithium metal chips (KGC Saintifik, Indonesia) on both sides. Before assembling the sintered pellet was polished with SiC paper until reach 0.6 mm of thickness. The symmetry cell was assembled within a coin cell 2032 in an argon glove box (stainless glove box series VGB-1, vacuum level −0.1 MPa) An Ultra-high purity argon gas (procured from Samator Gas, Indonesia) was used. After being rest for 4 h, an impedance measurement (EUCOL LCR meter, 20 Hz-5 MHz) was conducted. In this research, there was no heating treatment as it was conducted by previous research [17]. a Galvanostatic Charge—Discharge (GCD) (Corrtest Electrochemical Workstation) was then applied to the coin cell with a time-based mode, in which 60 s charging and 60 s discharging under 0.2 mA of current drawn. The GCD was conducted for 120 cycles (20-20-40-40). After each cycle, a Cyclic Voltammetry (Corrtest Electrochemical Workstation) test was conducted at 2 mV/s rates within voltage range of 2—4 V vs Li/Li$^+$.

3. Result and discussion

Zirconia powder used in this research has a different optical view as shown by the picture inserted in Fig. 1, along with their diffraction patterns. The diffraction patterns are compared with the standard diffraction of monoclinic zirconia ICSD#157403 and tetragonal ZrO$_2$ ICSD#157621. Fig. 1 shows that the diffraction pattern of ZrO$_2$(A) is in agreement with monoclinic ZrO$_2$, meanwhile, the diffraction pattern of ZrO$_2$(B) is in agreement with tetragonal ZrO$_2$, however, a small peak at 2θ 27.8° is not fit with t-ZrO$_2$. The peak is identified as cubic Na$_2$O based on a database of cubic Na$_2$O diffraction mp-2352 [18] under Cu radiation source. XRF analysis also confirms the presence of 13.36% Na within ZrO$_2$(B) as listed in Table 1. XRF analysis shows that Zr content in both is almost similar i.e., 47.94% and 48.45% for ZrO$_2$(A) and ZrO$_2$(B), respectively (Table 1).

ZrO$_2$(B) was prepared by caustic fusion of concentrated-zircon sand by applying a calcination temperature of 800 °C. Another research on preparing ZrO$_2$ from Indonesian zircon sand also found that at 800 °C the zirconia formed within a tetragonal structure [19]. Another study also found that monoclinic and tetragonal structures are reversibly formed under calcination temperature below 1170 °C [20]. Le Bail
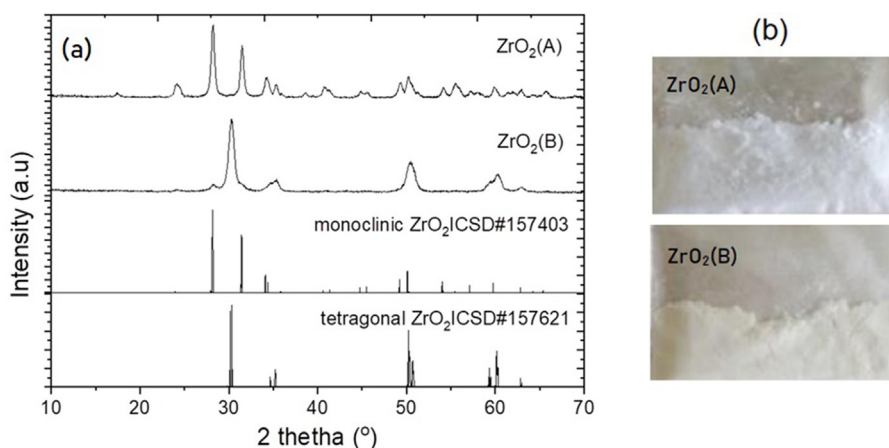

Fig. 1 — XRD patterns of ZrO$_2$(A) and ZrO$_2$(B) compared with standard diffraction of monoclinic ZrO$_2$ ICSD # 157403 and tetragonal ZrO$_2$ ICSD# 157621(a), and the optical images of each powder are depicted (b).

Table 1 — Elemental composition of ZrO$_2$ (A) and ZrO$_2$ (B) based on XRF analysis.

Element	Composition in ZrO$_2$ (A) (%)	Composition in ZrO$_2$ (B) (%)
Zr	47.94	48.45
O	27.17	27.60
Na	15.12	13.36
Mg	1.98	1.89
Si	0.95	1.60
La	0.80	0.93
Al	0.62	0.55

Table 2 — The refinement result of ZrO$_2$(A) and ZrO$_2$(B).

Cell parameters	ZrO$_2$(A)	ZrO$_2$(B)
Crystal structure and space group	monoclinic P 1 21/c 1	Tetragonal P 42/nmcS
a (Å)	5.06 (0)	3.6022 (9)
b (Å)	5.13 (0)	3.6022 (9)
c (Å)	5.23 (0)	5.190 (2)
V (Å^3)	134.13 (0)	67.34 (3)
A	90.0 (0)	90.0 (0)
B	99.265 (4)	90.0 (0)
γ	90.0 (0)	90.0 (0)
Rp (%)	5.32	6.89
Rwp (%)	5.53	7.54

refinement proceed well with a monoclinic structure for ZrO$_2$(A) and tetragonal structure for ZrO$_2$(B) with the cell parameters as listed in Table 2, and Le Bail plots are depicted in Fig. 2.

The Crystallite size of each ZrO$_2$ was determined by the Scherrer method, the results are 190.15 nm and 122.17 nm for m-ZrO$_2$ and t-ZrO$_2$, respectively. This is in agreement with another result that found the crystallite size of t-ZrO$_2$ is smaller than m-ZrO$_2$ [13], as it is also shown in Table 2 in which the volume cell of monoclinic ZrO$_2$ is higher than the tetragonal ZrO$_2$.

XRD patterns of the prepared LLZO (A) and LLZO (B) are depicted in Fig. 3, compared with the standard diffraction of tetragonal LLZO ICSD#246816 and standard diffraction of cubic LLZO ICSD#42259, and also with standard diffraction of m-ZrO$_2$ ICSD#157403. Le Bail refinement was conducted to LLZO (A) and proceed well with 3 phases of t-LLZO, m-LLZO, and m-ZrO$_2$ with %moles of composition 88.18%, 10.97%, and 2.85%, respectively, as listed in Table 3. Meanwhile, the Le Bail plots are depicted in Fig. 4. The mole ratio of cubic to tetragonal (c/t) structure is 0.124. It implies a low cubic content LLZO
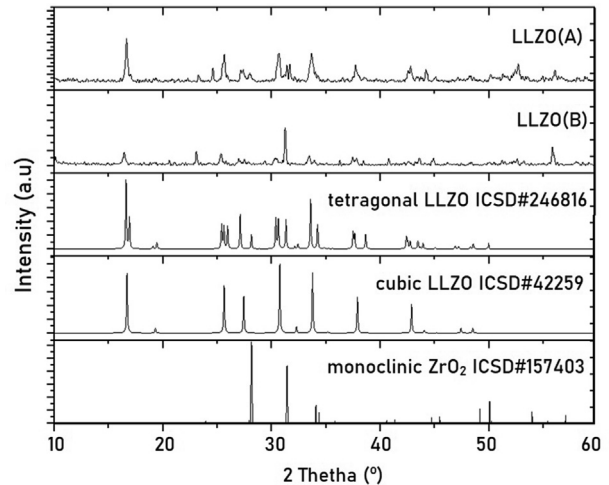
Fig. 3 — XRD patterns of LLZO(A) and LLZO(B) compare with t-LLZO ICSD#246816, c-LLZO ICSD#42259, and m-ZrO$_2$ ICSD#157403.

Table 3 — The refinement result of LLZO(A) that proceed well by submitting 3 phases of cubic LLZO ICSD#422259, tetragonal LLZO ICSD#246816, and monoclinic ZrO$_2$ ICSD#157403.

Cell parameters	LLZO(A)1000		
Structure/Space Group	t- LLZO/ P 41/a c d	c-LLZO/ Ia -3d	m- ZrO$_2$/ P 1 21/c 1
a (Å)	13.165 (2)	13.068 (1)	5.151 (2)
b (Å)	13.165 (2)	13.068 (1)	5.281 (5)
c (Å)	12.642 (3)	13.068 (1)	5.387 (6)
A	90	90	90
B	90	90	99.13 (5)
γ	90	90	90
% Molesse	88.18	10.97	2.85
Rp (%)	6.25		
Rwp (%)	9.93		

compare to the tetragonal structure, meanwhile, it is known that cubic structure provides higher lattice conductivity at RT than the tetragonal structure [11,21,22]. The proposed reaction mechanism is depicted in Eqs. (2) and (3).

$$Li_2CO_{3(s)} \xrightarrow{900°C} Li_2O_{(s)} + CO_{2(g)} \qquad (2)$$
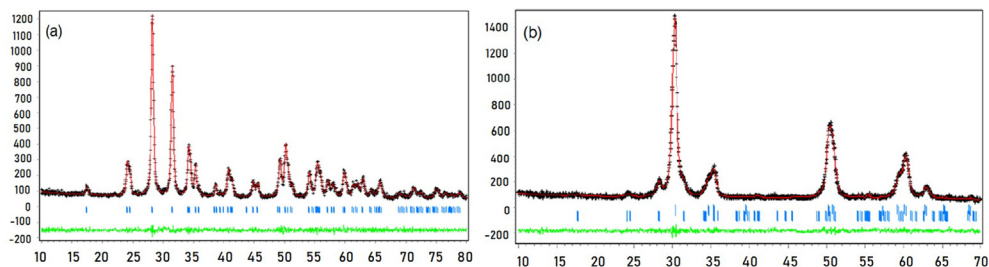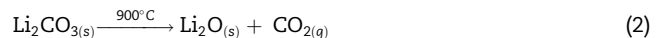
Fig. 2 — Le Bail plots of ZrO$_2$(A) and ZrO$_2$(B).
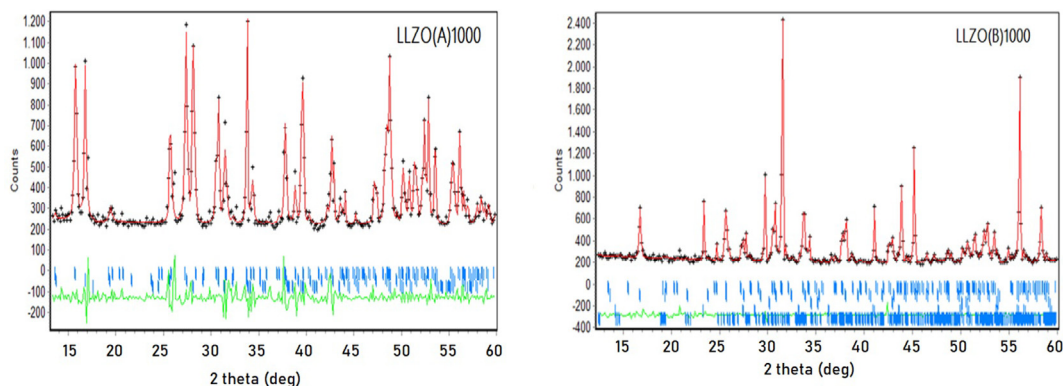
Fig. 4 – Le Bail plots of LLZO(A) and LLZO(B).

$$3.5Li_2O_{(s)} + 1.5La_2O_{3(s)} + 4ZrO_{2(s)} \rightarrow Li_7La_3Zr_2O_{12(s)} + 2ZrO_{2(s)} \tag{3}$$
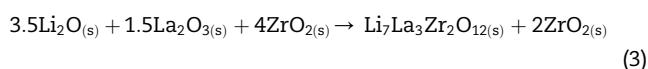
Meanwhile, Le Bail refinement of LLZO (B) did not proceed well with 3 phases of t-LLZO, c-LLZO, and t-ZrO₂. Two peaks at 2θ of 23.5° and 29.8° were not matched. Further, searching found that 23.5° is a specific peak of c-La₂Zr₂O₇, meanwhile, the peak at 29.8° belongs to triclinic-LiNaCO₃. The refinement results are listed in Table 4. The mole ratio c/t is 0.125, which is surprisingly close to the c/t of LLZO(A).

The secondary phase LiNaCO₃ was formed during calcination at 950 °C 6 h. XRF analysis as depicted in Table 1, confirms the presence of sodium within the ZrO₂ powder. The previous research found that sodium is present as disodium oxide, Na₂O [23]. During reaction at 950 °C, the sodium oxide reacted with carbon dioxide in the air, as proposed in the chemical reaction (Eq. (4)). The sodium carbonate is then involved within the reaction (Eq. (5)).

$$ZrO_{2(s)} + Na_2O_{(s)} + CO_{2(g)} \rightarrow ZrO_{2(s)} + Na_2CO_{3(s)} \tag{4}$$

$$4.5Li_2O_{(s)} + 2.5La_2O_{3(s)} + 5ZrO_{2(s)} + 2Na_2CO_{3(s)} \rightarrow Li_7La_3Zr_2O_{12(s)}$$
$$+ La_2Zr_2O_{7(s)} + ZrO_{2(s)} + 2LiNaCO_{3(s)} + Na_2O_{(s)} \tag{5}$$
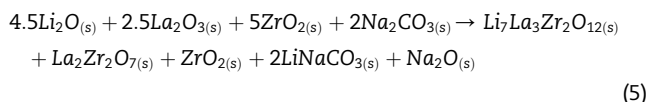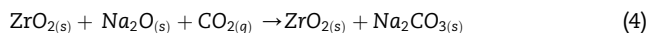
Sodium carbonate formation during heat treating reaction was not occurred in the m-ZrO₂, even though the powder also has a sodium content of 15.12%. The surface of monoclinic zirconia is known to be hydroxylated under ambient and in the most reactive atmosphere. The adsorbed-water molecules were then dissociated forming a Tribridge OH at tricoordinate oxygen of ZrO₂ [24]. The hydroxylation reduces interaction between Na in the zirconia powder with CO₂ in the air to form sodium carbonate. The absence of Na₂CO₃ seems to eliminate the production of LiNaCO₃.

SEM images of the prepared-LLZO are depicted in Fig. 5. The inserted images in Fig. 5 shows that LLZO (A) is a white-smooth powder, meanwhile, LLZO (B) is a brown-smooth powder. SEM analysis reveals a different surface morphology of both, in which the LLZO (A) shows a rough surface of rod shapes. Some are aggregates within a rough surface plate allowing a heterogeneous particle size. Meanwhile, LLZO (B) has a smooth surface morphology with some white spots of different size.

Raman analysis resulted spectra described in Fig. 6. Peaks at 100–150 cm^{-1} are mainly of La vibrational bands, 107 cm^{-1} and 121 cm^{-1} are T₂g and Eg La vibration [25]. The Li$^+$ ion bonding region are revealing at 361 cm^{-1} (T₂g), 410 cm^{-1} (Eg/T₂g), and 514 cm^{-1} (T₂g/Eg). Those Raman vibrations are in agreement with cubic garnet LLZO I_43d of space group [26]. A peak at 640 cm^{-1} belongs to Zr–O stretching [27]. LLZO (A) shows A1g t-LLZO at 640 cm^{-1} [28]. Meanwhile, LLZO (B) shows Eg symmetrical t-LLZO at 190 cm^{-1} [25], and T₂g t-LLZO at 712 cm^{-1} [28]. LLZO (A) also presents a peak at 1090 cm^{-1} belong to LiOH [29]. The peak also reveals at LLZO (B). It is probably the rest of lithium precursor which made bonding with hydroxide during calcination, as described by Eq. (6) [30].

Table 4 – The refinement result of LLZO(B) that proceed well by submitting 3 phases of cubic LLZO ICSD#422259, tetragonal LLZO ICSD#246816, tetragonal ZrO₂ ICSD#157403, La₂Zr₂O₇ and LiNaCO₃.

Cell parameters				LLZO(B)1000	
Crystal Structure Space Group	t- LLZO/P 41/a c d	c-LLZO/Ia -3 d	t- ZrO₂ P 1 21/c 1	c-La₂Zr₂O₇ Fd-3 m S	Triclinic-LiNaCO₃P1
a (Å)	13.104 (1)	12.940 (4)	3.606 (2)	10.779 (2)	14.120 (3)
b (Å)	13.104 (1)	12.940 (4)	3.606 (2)	10.779 (2)	13.986 (2)
c (Å)	12.649 (1)	12.940 (4)	5.190 (4)	10.779 (2)	3.3102 (3)
A	90	90	90	90	88.82 (1)
B	90	90	90	90	91.21 (1)
γ	90	90	90	90	118.839 (9)
% molesse	49.86	6.22	0.39	28.75	14.78
Rp (%)	1.91				
Rwp (%)	4.33				
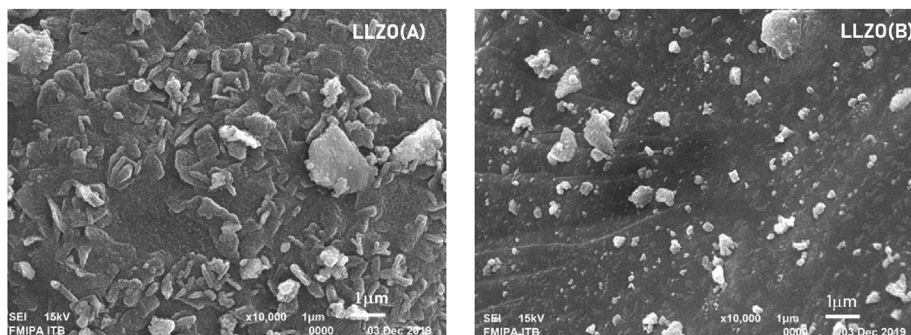
Fig. 5 – SEM images of LLZO(A) and LLZO(B).

LLZO (B) also provides a peak at 838 cm^{-1} belong to LiOH.H$_2$O [29] which probably formed during store the powder before analysis. The reversible water molecules adsorption to LiOH is depicted in Eq. (7) [30].

$$Li_2O + H_2O \Leftrightarrow 2LiOH \ (at \sim 400 - 500 \ °C) \qquad (6)$$

$$LiOH + H_2O \rightarrow LiOH.H_2O \qquad (7)$$
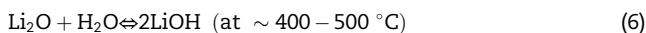
The rest of the ZrO$_2$ precursor also was detected within the sample. As it is shown in LLZO (A) a peak at around 300 cm^{-1} belongs to m-ZrO$_2$ [31]. The presence of m-ZrO$_2$ is in agreement with XRD analysis which found around 2.85 mol % of m-ZrO$_2$ exist within the LLZO (A) powder. Meanwhile, the tetragonal ZrO$_2$ precursor is also detected at 224 cm^{-1} and 636 cm^{-1} [31] as it is also detected by XRD refinement the presence of 0.85 mol % of t-ZrO$_2$ within the LLZO (B) powder. LLZO(B) also provides a peak at 980 cm^{-1} which is expected to be the vibration of linear carbonate, LiNaCO$_3$. The vibrational of linear carbonates are lying around 910–980 cm^{-1} [32].

Impedance analysis by blocking method found Nyquist plots as depicted in Fig. 7. Both materials show a single semicircle in which the impedance plot LLZO(B) falls into the smaller impedance value. Fitting of the impedance data with ZView (a software included within CS Studio 5, Corrtest Electrochemical Workstation) proceed well by applying the R–C network model as inserted in Fig. 7. The fitting result is listed in Table 5. The capacitance values of both materials which are 2.585×10^{-9} F and 6.048×10^{-9} for LLZO(A) and LLZO(B), respectively, confirm that the impedance values representing the grain boundary resistance. It is known that capacitance of around 1.4×10^{-9} F is related to grain-boundary impedance [14,33,34]. Both LLZO(A) and LLZO(B) have a (-6) order of ionic conductivity which are two orders lower than Al-doped-LLZO, which is 4×10^{-4} Scm^{-1} [35]. However, the order is close to the Al-doped LLZO which was synthesized by the co-precipitation method which is 2.80×10^{-6} Scm^{-1} [36], in which Al composition was 0.24 mol% to ensure pure cubic LLZO. However, material density seems to take a more significant role in the conductivity, proven by higher density ~96–98% provide higher ionic conductivity [35] than the lower density of ~80% [36]. It is also explained by other researchers that crystal microstructure including crystallite size, grain size, grain boundary, and bulk density affect the ionic conductivity of LLZO [25,37–39]. Even, Ta doped-LLZO which was synthesized by co-precipitation method and was sintered at 1000–1100 °C
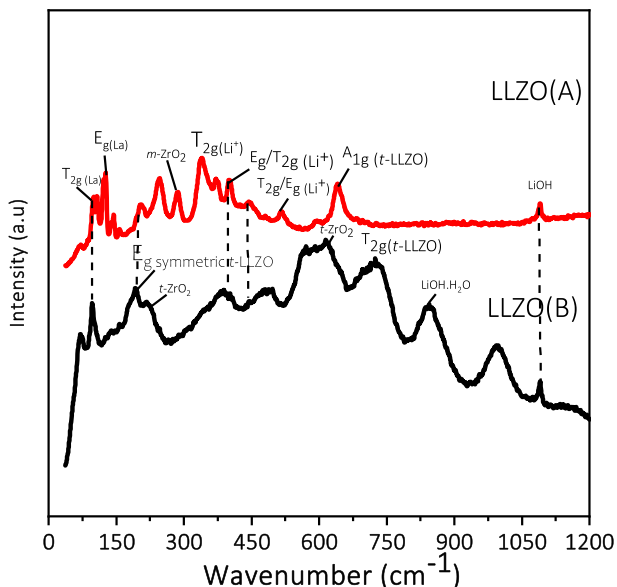

Fig. 6 – Raman spectra of LLZO (A) and LLZO(B).
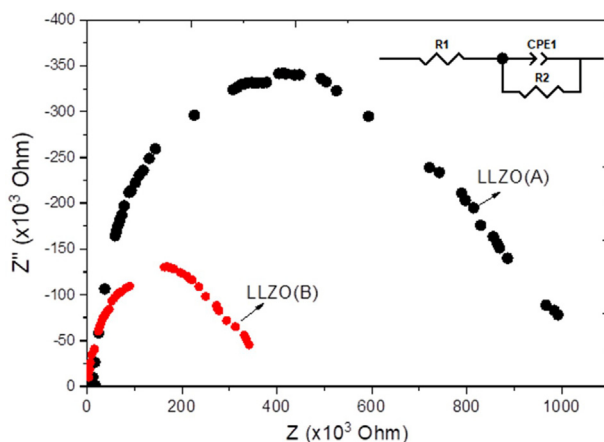

Fig. 7 – The Nyquist plot of silver blocking electrode LLZO(A) and LLZO(B) at room temperature.

Table 5 – The result of impedance data fitting of silver blocking electrode LLZO(A) and LLZO(B) at room temperature.

Materials	Resistance (kΩ)	CPE (Farads)	Material thickness (cm)	Active area of electrode (cm^2)	σ (Scm^{-1})
LLZO (A)	1219.190 ± 0.203	2.585×10^{-9}	0.317 ± 0.001	0.209 ± 0.0019	$1.245 \times 10^{-6} \pm 1.045 \times 10^{-8}$
LLZO (B)	458.115 ± 0.225	6.048×10^{-9}	0.145 ± 0.001	0.187 ± 0.0017	$1.647 \times 10^{-6} \pm 6.429 \times 10^{-9}$

for 16 h, provides only 7×10^{-6} Scm^{-1} because of low density. The density is 80% relative to the theoretical garnet LLZO [36]. Meanwhile, sintering at 1000 °C under Ar flow for 6 h for these two LLZO(A) and LLZO(B) in this research even produce lower relative density LLZO which are 67.24% and 68.58% for LLZO(A) and LLZO(B), respectively. Therefore, a study to increase the electrolyte density is an important thing to do next.

Considering the microstructure of LLZO(A) and LLZO(B) as well as the relative density of both which are almost similar, LLZO(B) shows a higher ionic conductivity than LLZO(A), as shown by Fig. 7 and Table 5. Even though the purity of LLZO(A) is higher than LLZO(B) as shown by fewer phase content, however the presence of LiNaCO$_3$ seems to contribute to the ionic conductivity. A study on a composite LiAlO$_3$–LiNaCO$_3$ solid electrolyte for solid oxide fuel cell found that Li$^+$, Na$^+$ and CO$_3^{2-}$ were mobile within the blocking silver system [40]. The AC impedance measurement analyzed all of the mobile ions, including M$^+$ (Li$^+$, Na$^+$) and CO$_3^{2-}$ which may contribute to the higher ion conductivity than others [40]. In addition, sintering at 1000 °C under Ar flow produced a major tetragonal phase whether with m-ZrO$_2$ or t-ZrO$_2$ as raw material. A minor cubic phase was produced at both result with the cubic-tetragonal ratio (c/t) almost similar i.e., 0.124 and 0.125 for LLZO(A) and LLZO(B), respectively. Another research found

that Li$_7$La$_3$Zr$_2$O$_{12}$ synthesis through sol–gel technique, has found formation of La$_2$Zr$_2$O$_7$ pyrochlore as major phase at 700 °C, and then further heating favors the pyrochlore LZ reacted with the residual lithium and lanthanum oxide to form tetragonal LLZO [12], which seems to occurred also in this research. Meanwhile, argon atmosphere seems to keep the CO$_3^{2-}$ availability within the system and increase the possibility to react with other cations such as Na$^+$ and Li$^+$ to form LiNaCO$_3$ (Table 4).

To understand the ionic conduction between cathode and anode material, a wafer of LCO-LLZO-mcmb was assembled and the impedance was measured. The Nyquist plots are depicted in Fig. 8 (a) (b), and the data are listed in Table 6 along with their capacitance (CPE, Farads) and their specific resistance (Ω cm^2). The specific resistance decreases as the temperature increases, in which at RT the specific resistance of LCO-LLZO(B)-mcmb is 18.99 Ωcm^2, lower than the specific resistance of LCO-LLZO(A)-mcmb which is 45.06 Ωcm^2. The resistance is even lower than the resistance of symmetrical Li-LLZO-Li at RT i.e., 500 Ωcm^2 [41] due to a thin-casted electrolyte that was vacuum dried seems to provided better contact between LCO-LLZO (A/B)-mcmb. The capacitance values of 1.250×10^{-8} F and 1.000×10^{-20} F corresponds to ionic conductivity of grain boundary and grain with the specific
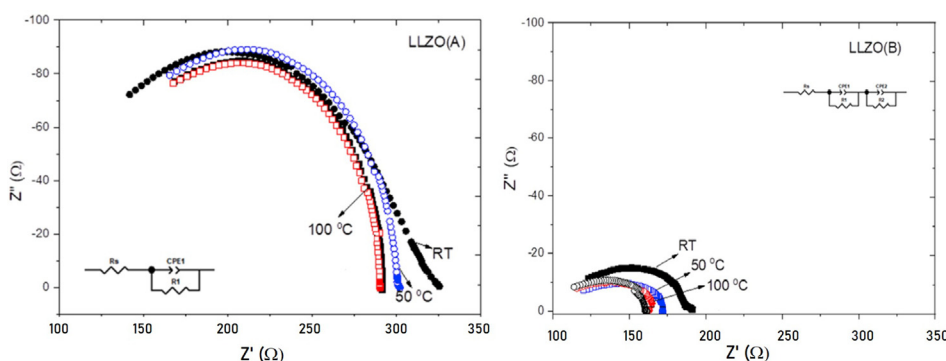
Fig. 8 – Nyquist plots of wafer LCO-SE-mcmb at various temperature.

Table 6 – Fitting result of the impedance data of LCO-Solid Electrolyte (SE)-mcmb at various temperature.

| Temperature (°C)	Resistance of LCO-SE-mcmb (Ω)		CPE (Farads)		Specific resistance of LCO-SE-mcmb (Ω cm^2)	
	LLZO(A)	LLZO(B)	LLZO(A)	LLZO(B)	LLZO(A)	LLZO(B)
RT	229.9 ± 0.023	28.24 ± 0.022	3.947×10^{-9}	1.250×10^{-8}	45.06 ± 0.055	18.99 ± 0.022
		68.69 ± 0.004		1.000×10^{-20}		
50	161.0 ± 0.017	16.48 ± 0.035	8.960×10^{-11}	7.053×10^{-9}	31.56 ± 0.028	17.64 ± 0.035
		73.52 ± 0.041		1.000×10^{-20}		
100	157.4 ± 0.017	22.86 ± 0.039	1.046×10^{-10}	2.822×10^{-10}	30.85 ± 0.016	15.71 ± 0.039
		57.29 ± 0.041		1.000×10^{-20}		
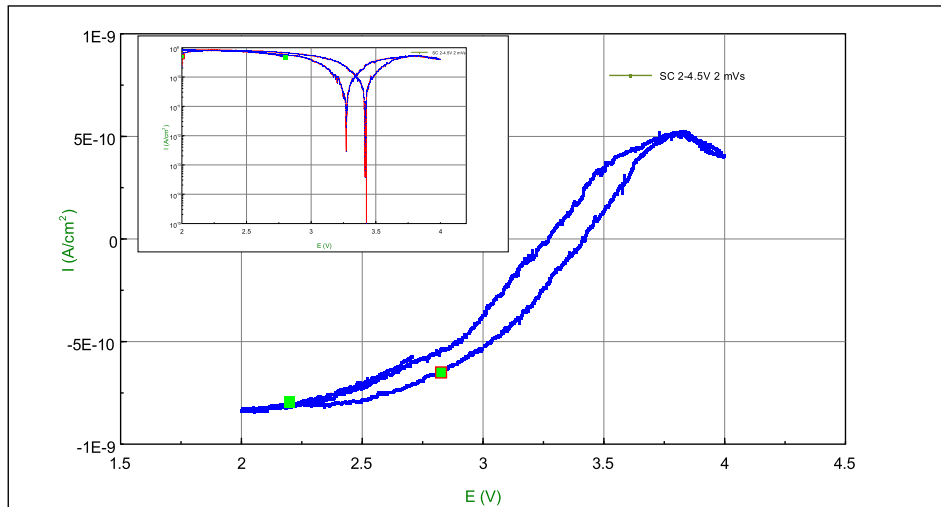
Fig. 9 − Cyclic Voltammogram of Li-LLZO(B)−Li at before cycling scan rate 2 mV/s.

conductivity value of 8.67×10^{-4} S/cm at RT. The bottom limit of 20 Hz seems to be not small enough to reveals the electronic resistance between SE-electrode, therefore there are no diffusion tails reveal in the Nyquist plots (Fig. 8), as was found by other researchers [42].

Based on its potential as solid electrolyte, it is important to understand the electrochemical behavior of LLZO(B) related to the Li and Li^+ ions. A cyclic voltammogram (Fig. 9) of the symmetrical cell Li-LLZO(B)−Li shows oxidation-reduction started at 3.3 V and 3.4 V, respectively. The inserted-Tafel plot of E vs log i confirms the redox potential clearly.

The Galvanostatic-Charge−Discharge curve as shown by Fig. 10(a) and (b) are relatively symmetrical, indicates that the

redox reaction on the electrode was reversible and the capacitive characteristic was steady [43]. The second-and third- 40 cycles are having a smaller capacity than the first-40 round (Fig. 10(b)), confirming by a smaller curve area. It confirmed the capacity degradation. Integrative data fitting with CS Studio 5 found that the specific capacity, Q is 0.0372 ± 0.0001 Ccm^{-2} at the 1st 40 cycles. It becomes 0.0299 ± 0.00012 Ccm^{-2} during the 2nd-40 cycles and remains constant during the 3rd-40 cycles. The low capacity of the prepared LLZO indicates a further treatment to increase the ionic conductivity of the LLZO is required before use as a solid electrolyte for LIB. Some modifications can be done such as single-doping with Ta [36], Gd [44], Ga [45], B [42,46], or double-doping such as Nb−Y [47].
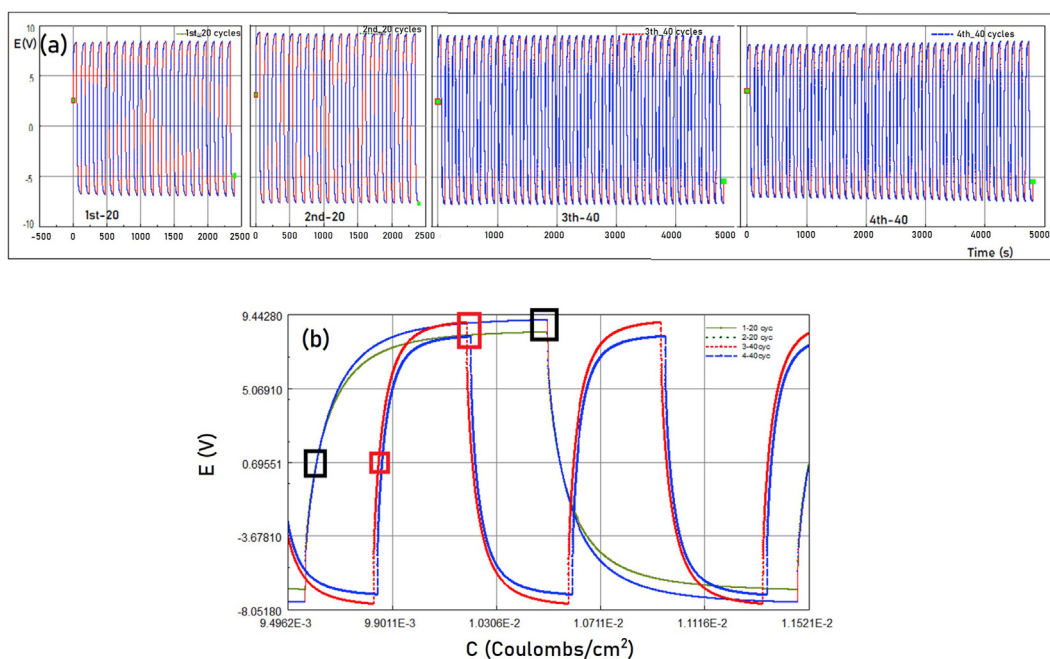

Fig. 10 − Galvanostatic cycling at 0.2 mA with 60 s charging and 60 s discharging (a), and the magnified crop (b).

4. Conclusion

This research found that a different crystal structure of ZrO_2 precursors produced similar LLZO structures which are tetragonal and cubic, and surprisingly with a similar cubic-to-tetragonal ratio (c/t) of 0.124—0.125. However, different-secondary phases are found. The presence of triclinic $LiNaCO_3$ phase within the LLZO synthesized from t-ZrO_2 (LLZO(B)), seems to provide an advantage by a higher single-LLZO ionic conductivity and also a lower specific resistance in between anode and cathode material, i.e mcmb and LCO. The prepared-LLZO(B) provides a reversible oxidation-reduction at around 3.3 V vs Li/Li$^+$ with a specific capacity, Q (Ccm^{-2}) drops at around 16.6% after 40 charge—discharge cyclings, and it remains constant for the next 2nd- and 3rd- 40 cycles. It indicates the need to improves its electrochemical properties before being used as a solid electrolyte for lithium-ion batteries.

Declaration of Competing Interest

The authors declare that they have no known competing financial interests or personal relationships that could have appeared to influence the work reported in this paper.

Acknowledgements

REFERENCES

[1] Li HY, Huang B, Huang Z, Wang CA. Enhanced mechanical strength and ionic conductivity of LLZO solid electrolytes by oscillatory pressure sintering. Ceram Int 2019;45:18115—8. https://doi.org/10.1016/j.ceramint.2019.05.241.

[2] Wang L, Zhao X, Dai S, Shen Y, Wang M. High-rate and stable iron phosphide nanorods anode for sodium-ion battery. Electrochim Acta 2019;314:142—50. https://doi.org/10.1016/j.electacta.2019.05.071.

[3] Oh DY, Kim DH, Jung SH, Han JG, Choi NS, Jung YS. Single-step wet-chemical fabrication of sheet-type electrodes from solid-electrolyte precursors for all-solid-state lithium-ion batteries. J Mater Chem A 2017;5:20771—9. https://doi.org/10.1039/c7ta06873e.

[4] Hou W, Guo X, Shen X, Amine K, Yu H, Lu J. Nano Energy Solid electrolytes and interfaces in all-solid-state sodium batteries : progress and perspective. Nano Energy 2018;52:279—91. https://doi.org/10.1016/j.nanoen.2018.07.036.

[5] Xu L, Tang S, Cheng Y, Wang K, Liang J, Liu C, et al. Interfaces in solid-state lithium batteries. Joule 2018;2:1991—2015. https://doi.org/10.1016/j.joule.2018.07.009.

[6] Wu Z, Xie Z, Yoshida A, Wang Z, Hao X, Abudula A, et al. Utmost limits of various solid electrolytes in all-solid-state lithium batteries: a critical review. Renew Sustain Energy Rev 2019;109:367—85. https://doi.org/10.1016/j.rser.2019.04.035.

[7] Murugan R, Thangadurai V, Weppner W. Fast lithium ion conduction in garnet-type $Li_7La_3Zr_2O_{12}$. Angew Chemie - Int Ed 2007;46:7778—81. https://doi.org/10.1002/anie.200701144.

[8] Ramakumar S, Deviannapoorani C, Dhivya L, Shankar LS, Murugan R. Lithium garnets: synthesis, structure, Li+ conductivity, Li+ dynamics and applications. Prog Mater Sci 2017;88:325—411. https://doi.org/10.1016/j.pmatsci.2017.04.007.

[9] Kokal I, Somer M, Notten PHL, Hintzen HT. Sol-gel synthesis and lithium ion conductivity of $Li_7La_3Zr_2O_{12}$ with garnet-related type structure. Solid State Ionics 2011;185:42—6. https://doi.org/10.1016/j.ssi.2011.01.002.

[10] Shao C, Liu H, Yu Z, Zheng Z, Sun N, Diao C. Structure and ionic conductivity of cubic $Li_7La_3Zr_2O_{12}$ solid electrolyte prepared by chemical co-precipitation method. Solid State Ionics 2016;287:13—6. https://doi.org/10.1016/j.ssi.2016.01.042.

[11] Kotobuki M, Kanamura K, Sato Y, Yamamoto K, Yoshida T. Electrochemical properties of $Li_7La_3Zr_2O_{12}$ solid electrolyte prepared in argon atmosphere. J Power Sources 2012;199:346—9. https://doi.org/10.1016/j.jpowsour.2011.10.060.

[12] Deviannapoorani C, Ramakumar S, Janani N, Murugan R. Synthesis of lithium garnets from $La_2Zr_2O_7$ pyrochlore. Solid State Ionics 2015;283:123—30. https://doi.org/10.1016/j.ssi.2015.10.006.

[13] Wang D, Zhong G, Pang WK, Guo Z, Li Y, McDonald MJ, et al. Toward understanding the lithium transport mechanism in garnet-type solid electrolytes: Li$^+$ ion exchanges and their mobility at octahedral/tetrahedral sites. Chem Mater 2015;27:6650—9. https://doi.org/10.1021/acs.chemmater.5b02429.

[14] Apriany K, Permadani I, Syarif DG, Soepriyanto S, Rahmawati F. Electrical conductivity of zirconia and yttrium-doped zirconia from Indonesian local zircon as prospective material for fuel cells. IOP Conf Ser Mater Sci Eng 2016;107. https://doi.org/10.1088/1757-899X/107/1/012023.

[15] Patterson A. The Scherrer formula for X-ray particle size determination. Phys Rev J Arch 1939;56:978. https://doi.org/10.1103/PhysRev.56.978.

[16] Natalia V, Rahmawati F, Wulandari A, Purwanto A. Graphite/Li_2ZrO_3 anode for a $LiFePO_4$ battery. Chem Pap 2019;73:757—66. https://doi.org/10.1007/s11696-018-0626-0.

[17] Sharafi A, Yu S, Naguib M, Lee M, Ma C, Meyer HM, et al. Impact of air exposure and surface chemistry on Li-$Li_7La_3Zr_2O_{12}$ interfacial resistance. J Mater Chem A 2017;5:13475—87. https://doi.org/10.1039/c7ta03162a.

[18] Persson K. Materials data on Na_2O (SG:225) by materials project. Mater Proj 2014. https://doi.org/10.17188/1199567.

[19] Musyarofah, Lestari ND, Nurlaila R, Muwwaqor NF, Triwikantoro Pratapa S. Synthesis of high-purity zircon, zirconia, and silica nanopowders from local zircon sand. Ceram Int 2019;45:6639—47. https://doi.org/10.1016/j.ceramint.2018.12.152.

[20] Mihai LL, Parlatescu I, Gheorghe C, Andreescu C, Bechir A, Pacurar M, et al. In vitro study of the effectiveness to fractures of the aesthetic fixed restorations achieved from zirconium and alumina. Rev Chim 2014;65:725—9.

[21] Shimonishi Y, Toda A, Zhang T, Hirano A, Imanishi N, Yamamoto O, et al. Synthesis of garnet-type $Li_{7-x}La_3Zr_2O_{12-1/2x}$ and its stability in aqueous solutions. Solid State Ionics 2011;183:48—53. https://doi.org/10.1016/j.ssi.2010.12.010.

[22] Thompson T. Tetragonal vs. cubic phase stability in Al − free Ta doped $Li_7La_3Zr_2O_{12}$ (LLZO). J Mater Chem A 2014;12:13431. https://doi.org/10.1039/C4TA02099E.

[23] Rahmawati F, Heraldy E. Double steps leaching and filtration in caustic fusion method to produce zirconia from local zircon concentrate 201499–102; 2014. https://doi.org/10.2991/icopia-14.2015.18.

[24] Kouva S, Honkala K, Lefferts L, Kanervoa J. Review: monoclinic zirconia, its surface sites and their interaction with carbon monoxide. Catal Sci Technol 2015. https://doi.org/10.1039/C5CY00330J.

[25] Kumar PJ, Nishimura K, Senna M, Düvel A, Heitjans P, Kawaguchi T. A novel low-temperature solid-state route for nanostructured cubic garnet $Li_7La_3Zr_2O_{12}$ and its application to Li-ion battery. RSC Adv 2016;6:62656–67. https://doi.org/10.1039/c6ra09695f.

[26] Alodia Orera A, Larraz G, Rodríguez-Velamazán J, Campo J, Sanjuán A, Luisa M. Influence of Li^+ and H^+ distribution on the crystal structure of $Li_{7-x}H_xLa_3Zr_2O_{12}$ ($0 \leq x \leq 5$) garnets. Inorg Chem 2016;55:1324–32. https://doi.org/10.1021/acs.inorgchem.5b02708.

[27] Larraz G, Orera A, Sanjuán ML. Cubic phases of garnet-type $Li_7La_3Zr_2O_{12}$: the role of hydration. J Mater Chem A 2013;1:11419–28. https://doi.org/10.1039/c3ta11996c.

[28] Tietz F, Wegener T, Gerhards MT, Giarola M, Mariotto G. Synthesis and Raman micro-spectroscopy investigation of $Li_7La_3Zr_2O_{12}$. Solid State Ionics 2013;230:77–82. https://doi.org/10.1016/j.ssi.2012.10.021.

[29] Gorelik VS, Bi D, Voinov YP, Vodchits AI, Gorshunov BP, Yurasov NI, et al. Raman spectra of lithium compounds. J Phys Conf Ser 2017;918. https://doi.org/10.1088/1742-6596/918/1/012035.

[30] Geng H, Chen K, Yi D, Mei A, Huang M, Lin Y, et al. Formation mechanism of garnet-like $Li_7La_3Zr_2O_{12}$ powder prepared by solid state reaction. Xiyou Jinshu Cailiao Yu Gongcheng/Rare Met Mater Eng 2016;45:612–6. https://doi.org/10.1016/s1875-5372(16)30081-9.

[31] Basahel SN, Ali TT, Mokhtar M, Narasimharao K. Influence of crystal structure of nanosized ZrO_2 on photocatalytic degradation of methyl orange. Nanoscale Res Lett 2015;10. https://doi.org/10.1186/s11671-015-0780-z.

[32] Cresce AV, Russell SM, Borodin O, Allen JA, Schroeder MA, Dai M, et al. Solvation behavior of carbonate-based electrolytes in sodium ion batteries. Phys Chem Chem Phys 2017;19:574–86. https://doi.org/10.1039/c6cp07215a.

[33] Rahmawati F, Prijamboedi B, Soepriyanto S, Ismunandar. SOFC composite electrolyte based on LSGM-8282 and zirconia or doped zirconia from zircon concentrate. Int J Miner Metall Mater 2012;19:863–71. https://doi.org/10.1007/s12613-012-0640-0.

[34] Martin P, Carlos Pico L, Li Veiga L. $(4-x)/3Ti_{(5-2x)/3}Cr_xO_4$ ($0 \leq x \leq 0.9$) spinels: new negatives for lithium batteries. Solid State Sci 2007;9:521–6. https://doi.org/10.1016/j.solidstatesciences.2007.03.023.

[35] Rangasamy E, Wolfenstine J, Sakamoto J. The role of Al and Li concentration on the formation of cubic garnet solid electrolyte of nominal composition $Li_7La_3Zr_2O_{12}$. Solid State Ionics 2012;206:28–32. https://doi.org/10.1016/j.ssi.2011.10.022.

[36] Zhang X, Fergus J. Phase content and conductivity of aluminum- and tantalum-doped garnet-type lithium lanthanum zirconate solid electrolyte materials. ECS Trans 2017;77:509–16. https://doi.org/10.1149/07711.0509ecst.

[37] Botros M, Djenadic R, Clemens O, Möller M, Hahn H. Field assisted sintering of fine-grained $Li_{7-3x}La_3Zr_2Al_xO_{12}$ solid electrolyte and the influence of the microstructure on the electrochemical performance. J Power Sources 2016;309:108–15. https://doi.org/10.1016/j.jpowsour.2016.01.086.

[38] Cheng L, Chen W, Kunz M, Persson K, Tamura N, Chen G, et al. Effect of surface microstructure on electrochemical performance of garnet solid electrolytes. ACS Appl Mater Interfaces 2015. https://doi.org/10.1021/am508111r.

[39] Liu Q, Geng Z, Han C, Fu Y, Li S, He Y bing, et al. Challenges and perspectives of garnet solid electrolytes for all solid-state lithium batteries. J Power Sources 2018;389:120–34. https://doi.org/10.1016/j.jpowsour.2018.04.019.

[40] Raza R, Gao Z, Singh T, Singh G, Li S, Zhu B. $LiAlO_2$-$LiNaCO_3$ composite electrolyte for solid oxide fuel cells. J Nanosci Nanotechnol 2011;11:5402–7. https://doi.org/10.1166/jnn.2011.3784.

[41] Sharafi A, Kazyak E, Davis AL, Yu S, Thompson T, Siegel DJ, et al. Surface chemistry mechanism of ultra-low interfacial resistance in the solid-state electrolyte $Li_7La_3Zr_2O_{12}$. Chem Mater 2017;29:7961–8. https://doi.org/10.1021/acs.chemmater.7b03002.

[42] Ohta S, Komagata S, Seki J, Saeki T, Morishita S, Asaoka T. Short communication All-solid-state lithium ion battery using garnet-type oxide and Li_3BO_3 solid electrolytes fabricated by screen-printing. J Power Sources 2013;238:53–6. https://doi.org/10.1016/j.jpowsour.2013.02.073.

[43] Qian S, Chen X, Jiang S, Pan Q, Gao Y, Wang L, et al. Direct detection of charge and discharge process in supercapacitor by fiber-optic LSPR sensors. Nanophotonics 2020;9:1071–9. https://doi.org/10.1515/nanoph-2019-0504.

[44] Song S, Chen B, Ruan Y, Sun J, Yu L, Wang Y, et al. Gd-doped $Li_7La_3Zr_2O_{12}$ garnet-type solid electrolytes for all-solid-state Li-Ion batteries. Electrochim Acta 2018;270:501–8. https://doi.org/10.1016/j.electacta.2018.03.101.

[45] Su J, Huang X, Song Z, Xiu T, Badding ME, Jin J, et al. Overcoming the abnormal grain growth in Ga-doped $Li_7La_3Zr_2O_{12}$ to enhance the electrochemical stability against Li metal. Ceram Int 2019;45:14991–6. https://doi.org/10.1016/j.ceramint.2019.04.236.

[46] Alaih I, Fathonah S, Rahmawati F, Nugrahaningtyas K. Addition of calcined $Na_2B_4O_7$ on the synthesis of $Li_7La_3Zr_2O_{12}$. J Kim Sains Dan Apl 2021;24:77–84. https://doi.org/10.14710/jksa.24.3.77-84.

[47] Gai J, Zhao E, Ma F, Sun D, Ma X, Jin Y, et al. Improving the Li-ion conductivity and air stability of cubic $Li_7La_3Zr_2O_{12}$ by the co-doping of Nb, Y on the Zr site. J Eur Ceram Soc 2018;38:1673–8. https://doi.org/10.1016/j.jeurceramsoc.2017.12.002.